Magnetic and magnetoelastic properties of Er_3Al_2

Gorbunov, D.; Palazzese Di Basilio, S.; Ishii, I.; Andreev, A. V.; Sebek, J.; Buturlim, V.; Suzuki, T.; Zherlitsyn, S.; Wosnitza, J.;

Originally published:

August 2022

Physical Review Materials 6(2022), 084409

DOI: https://doi.org/10.1103/PhysRevMaterials.6.084409

Magnetic and magnetoelastic properties of Er_3Al_2

D. I. Gorbunov,[1] S. Palazzese,[1,2] I. Ishii,[3] A. V. Andreev,[4]
J. Šebek,[4] V. Buturlim,[5] T. Suzuki,[3] S. Zherlitsyn,[1] and J. Wosnitza[1,2]

[1]*Hochfeld-Magnetlabor Dresden (HLD-EMFL) and Würzburg-Dresden Cluster of Excellence ct.qmat, Helmholtz-Zentrum Dresden-Rossendorf, 01328 Dresden, Germany*
[2]*Institut für Festkörper- und Materialphysik, TU Dresden, 01062 Dresden, Germany*
[3]*Department of Quantum Matter, AdSE, Hiroshima University*
[4]*Institute of Physics, Academy of Sciences, Na Slovance 2, 182 21 Prague, Czech Republic*
[5]*Charles University, Faculty of Mathematics and Physics, Department of Condensed Matter Physics, Ke Karlovu 5, Prague 121 16, Czech Republic*

We report on comprehensive investigations of Er_3Al_2 exhibiting a number of magnetic states. We observe three spontaneous antiferromagnetic transitions at 10, 14, and 24 K. Furthermore, our high-field magnetization and sound-velocity measurements reveal a number of crystal-electric-field (CEF) transitions. Additionally, the velocity of transverse acoustic waves shows a pronounced softening with decreasing temperature in the paramagnetic state. A CEF model that includes quadrupolar interactions explains the observed magnetic and elastic properties and provides a CEF scheme of Er_3Al_2. However, to explain some of the observations, a refined, more sophisticated model needs to be developed.

I. INTRODUCTION

Rare-earth-based compounds with nonmagnetic metals display a rich variety of electronic properties enabling studies of exchange interactions and their frustration, crystal electric fields, critical and strongly correlated electron phenomena, and superconductivity (see, e.g., Refs. [1–4]). The interest in these materials is further enhanced by the fact that most rare-earth elements have well-localized $4f$ electrons making these compounds model systems to test the validity of existing theories.

The magnetic properties of rare-earth-based materials can be understood in terms of exchange interactions and magnetocrystalline anisotropy. The involved exchange interactions are of the Ruderman-Kittel-Kasuya-Yosida (RKKY) type, mediated from one magnetic ion to another through the conduction electrons. The long-range oscillatory character of these interactions frequently leads to a competition between positive and negative interionic couplings, which often produces incommensurate magnetic structures [5–8].

The magnetocrystalline anisotropy is observed by the preference of the magnetization to be oriented along a specific crystallographic direction. The anisotropy arises due to an electrostatic interaction between the aspherical $4f$ charge cloud and surrounding charges, i.e., the crystal electric field (CEF). The CEF plays a preponderant role in the magnetic, thermal, elastic, and other physical properties associated with rare-earth magnetism [9–11].

A competition between exchange and anisotropy interactions can lead to complex magnetic states. The antiferromagnet Er_3Al_2, for example, displays three magnetic phase transitions below 30 K [12, 13]. At the Néel temperature, $T_{N1} = 27.4$ K, part of the Er moments order along the tetragonal [001] axis, as found for a polycrystal. Two further transitions occur at $T_{N2} = 19.3$ K and $T_{N3} = 12.6$ K where the remaining Er moments order close to or within the basal plane of the unit cell. No other information is available for Er_3Al_2, although the large number of magnetic transitions calls for a more detailed examination of its magnetic and other electronic properties.

Here, we report on a combined study of the magnetization, magnetic susceptibility, specific heat, and ultrasound properties of an Er_3Al_2 single crystal. We observe three antiferromagnetic transitions as a function of temperature at 10, 14, and 24 K. Magnetization and sound-velocity measurements in pulsed magnetic fields up to 58 T reveal a number of anomalies, some of which can be explained by CEF effects. The sound velocity of transverse acoustic waves shows a pronounced softening with decreasing temperature in the paramagnetic state. A CEF model that includes quadrupolar interactions explains the temperature and field dependences of the magnetic and elastic properties of Er_3Al_2. However, this analysis does not reproduce all anomalies, and a refined model is necessary to explain them.

II. EXPERIMENTAL DETAILS

An Er_3Al_2 single crystal was grown by a modified Czochralski method from a stoichiometric mixture of the pure elements (99.9% Er, 99.999% Al) in a tri-arc furnace on a water-cooled Cu crucible under protective Ar atmosphere. The lattice parameters of the tetragonal crystal structure (space group $P4_2/mnm$) are $a = 8.127$ Å and $c = 7.492$ Å, in good agreement with previous studies [12, 13]. Back-scattered Laue diffraction was used to check the single-crystalline state and to orient the crystal for magnetization, magnetic-susceptibility, specific-heat, and ultrasound measurements.

Energy Dispersive X-Ray Analysis was performed using a scanning electron microscope Tescan MIRA 3. It confirmed the single phase character of the investigated Er_3Al_2 crystal yielding 61.9 at.% : 38.1 at.% for the con-

centrations of the elements Er : Al, which is in good agreement with the ideal ratio (the error is 2 at.%).

Magnetization and magnetic susceptibility in static magnetic fields up to 14 T were measured between 2 and 300 K using a commercial Physical Property Measurement System (PPMS). For the magnetic-susceptibility measurements, we applied an ac-excitation field, $\mu_0 H_{\rm exc}$ = 0.5 mT, at a frequency of 87 Hz. The PPMS was also used for specific-heat measurements utilizing the relaxation method.

High-field magnetization was measured in pulsed magnetic fields up to 58 T by the induction method using a coaxial pick-up coil system (a detailed description of the magnetometer can be found in Ref. [14]). Absolute values of the magnetization were calibrated using data obtained in static fields.

The field and temperature dependences of the relative sound-velocity changes, $\Delta v/v$, were measured using an ultrasound pulse-echo technique [15, 16]. A pair of piezoelectric transducers were glued to opposite surfaces of the sample in order to excite and detect acoustic waves. We measured the longitudinal, $\boldsymbol{k}$ || $\boldsymbol{u}$ || [110] [$(C_{11}+C_{12}+2C_{66})/2$], and transverse, $\boldsymbol{k}$ || [110], $\boldsymbol{u}$ || [001] (C_{44}) and $\boldsymbol{k}$ || [110], $\boldsymbol{u}$ || [1 − 10] [$(C_{11}-C_{12})/2$] acoustic modes. Here, $\boldsymbol{k}$ and $\boldsymbol{u}$ are the wavevector and polarization of the acoustic waves, respectively.

III. RESULTS AND DISCUSSION

The magnetic susceptibility, χ, of Er_3Al_2 shows a shoulder at $T_{\rm N2}$ = 14 K and a pronounced maximum at $T_{\rm N3}$ = 10 K when $H_{\rm exc}$ is applied along the [100] and [110] axes [Fig. 1(a)]. In a neutron-diffraction study, the Er moments were found to order close to the basal plane at $T_{\rm N2}$ and $T_{\rm N3}$ [13]. For $\boldsymbol{H}_{\rm exc}$ || [001], χ starts to decrease at $T_{\rm N1}$ = 24 K. For this field orientation, one also observes a small kink at $T_{\rm N3}$ = 10 K.

The specific heat, C, shows anomalies at $T_{\rm N1}$, $T_{\rm N2}$, and $T_{\rm N3}$ corresponding to second-order phase transitions [Fig. 1(b)]. Our Néel-temperature values are lower by several Kelvin as compared to those reported in Ref. [13], possibly due to a slightly different composition.

Below 30 K, relative sound-velocity changes, $\Delta v/v$, show features that evidence enlarged magnetoelastic coupling [Fig. 1(c)]. For the longitudinal mode $(C_{11}+C_{12}+2C_{66})/2$, $\Delta v/v$ displays a local minimum at $T_{\rm N1}$. Around this temperature, $\Delta v/v$ for the transverse modes C_{44} and $(C_{11}-C_{12})/2$ shows a pronounced softening. In the vicinity of $T_{\rm N2}$ and $T_{\rm N3}$, minima in the sound velocity appear for C_{44} and $(C_{11}-C_{12})/2$.

Our high-field magnetization data show a large magnetic anisotropy for field applied within the basal plane and along the [001] axis [Fig. 2(a)]. The [100] axis is the easy magnetization direction. In fields up to 6 T applied along the easy axis, one observes a non-monotonous increase in the magnetization, M [inset in Fig. 2(a)]. The field derivative of the magnetization, dM/dH, shows two

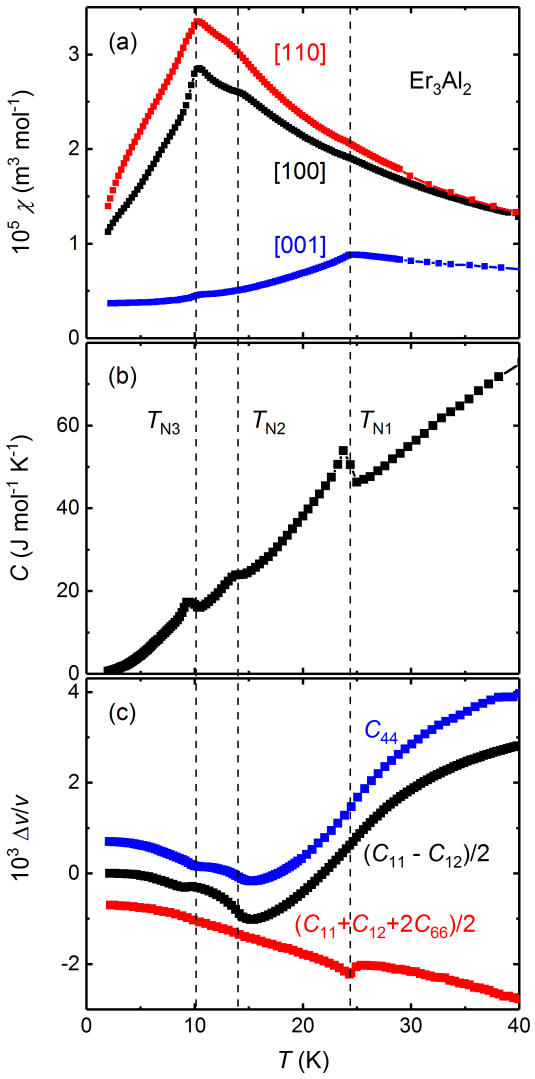

FIG. 1: Temperature dependences of (a) the magnetic susceptibility, χ, (b) specific heat, C, and (c) relative sound velocity, $\Delta v/v$, of longitudinal and transverse acoustic waves in Er_3Al_2. The ultrasound frequencies were 61.2, 102.8, and 36.3 MHz for the modes C_{44}, $(C_{11}-C_{12})/2$, and $(C_{11}+C_{12}+2C_{66})/2$, respectively. In panel (c), the curves are vertically shifted for clarity.

maxima at 0.9 and 2.4 T. In the highest applied field, the total magnetization approaches $3 \times M_{\rm Er}$ = 27 $\mu_{\rm B}$, where $M_{\rm Er} = g_j J \mu_{\rm B}$ = 9 $\mu_{\rm B}$ is the saturated magnetic moment per Er atom. Here, g_j = 1.2 and J = 15/2 are the Landé factor and the quantum number of the total angular momentum of a Er^{3+} ion, respectively. It should be noted that an additional non-negligible contribution may be given by the conduction electrons polarized by the localized $4f$ states. There is also anisotropy within the basal plane since Er_3Al_2 shows a different magnetization process when field is applied along the [110] axis. In particular, a weak S-shape is evident between 10 and 20 T. The [001] axis is the hard magnetization direction. For field applied along this axis, a field-induced transition

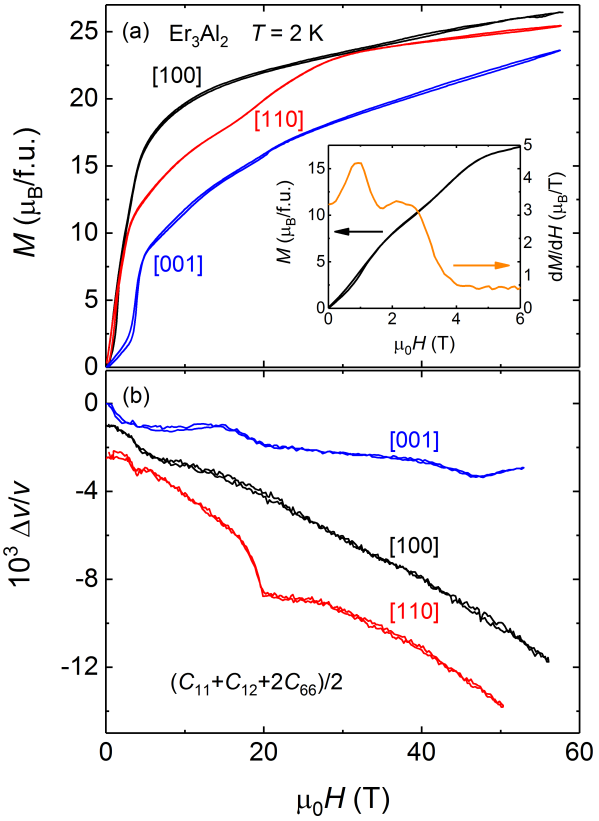

FIG. 2: Field dependences of (a) the magnetization, M, and (b) relative sound velocity, $\Delta v/v$, of longitudinal acoustic waves for field applied along the principal crystallographic directions of Er_3Al_2 at 2 K. The inset in panel (a) shows M and its field derivative, dM/dH, for field applied along the [100] axis up to 6 T. The ultrasound frequencies were 36, 42, and 82 MHz for field applied along the [100], [110], and [001] axes, respectively. In panel (b), the curves are vertically shifted for clarity.

is observed just below 4 T.

Our magnetization measurements reveal that the Er magnetic moments lie predominantly in the basal plane at 2 K, in agreement with the earlier neutron-scattering data [13]. According to those microscopic data, two Er sites have their magnetic moments confined to the basal plane below T_{N3}. Between T_{N1} and T_{N2}, the third Er site carries an ordered magnetic moment aligned along the [001] axis. Our results show no change of the easy magnetization direction with temperature. We observe no anomalies in χ, C, and $\Delta v/v$ other than those at T_{N1}, T_{N2}, and T_{N3} (Fig. 1). Additionally, χ is substantially smaller when the excitation field is applied along the [001] axis than along the basal-plane directions [Fig. 1(a)]. Further, our high-field magnetization measurements [see Figs. 3(a), (b), and (c) below] show no change of the easy direction above 2 K. Based on these experimental results, we conclude that the Er magnetic moments align close to the basal plane in the whole temperature range of the magnetically ordered states.

The sound velocity of the acoustic mode $(C_{11}+C_{12}+2C_{66})/2$ softens in field applied along all directions [Fig. 2(b)]. Broad and narrow features are observed in $\Delta v/v$ for $\boldsymbol{H}$ || [100] and $\boldsymbol{H}$ || [110], respectively, below 10 T. For $\boldsymbol{H}$ || [110], additional softening is evident upon approaching 20 T, i.e., in the same field range where the S-shape emerges in the magnetization [Fig. 2(a)]. A change of slope can also be resolved in the $\Delta v/v$ vs. H dependence between 10 and 20 T for field applied along the [001] axis.

In order to gain more information on the field-induced anomalies, we performed magnetization and ultrasound measurements at various elevated temperatures. The slope of the magnetization for $\boldsymbol{H}$ || [100] decreases below 20 T with increasing temperature [Fig. 3(a)]. The H dependence of $\Delta v/v$ for this field direction hardly changes with temperature [Fig. 3(d)]. For $\boldsymbol{H}$ || [110], the low- and high-field anomalies in the magnetization and sound velocity gradually disappear upon approaching 25 K [Figs. 3(b) and (e)]. Remarkably, the critical field of the anomalies for field applied along the basal plane directions does not change with temperature. This suggests that these anomalies are due to CEF transitions (level crossings). For $\boldsymbol{H}$ || [001], the jump in the magnetization below 4 T smears out and becomes S-shaped above 15 K [Fig. 3(c)]. The maximum in $\Delta v/v$ between 10 and 20 T disappears above 10 K [Fig. 3(f)]. At 10 K, the field dependence of the sound velocity shows a minimum at 28 T, the origin of which is not clear. The data at 15 K has no anomalies, whereas a minimum at 6 T emerges at 20 K. The observed temperature evolution of the field-dependent sound velocity likely suggests that, apart from the CEF transitions, magnetic moment rotations significantly affect the elastic properties of Er_3Al_2 when field is applied along the hard [001] axis.

Assuming that some of the field-induced anomalies are due to CEF effects, below we use a CEF model for analyzing our data in the paramagnetic state (analysis of the antiferromagnetic state requires exchange coupling constants which are not known). This first analysis of the magnetic and elastic properties assumes a single site of Er^{3+} in the crystal lattice of Er_3Al_2. We have done calculations for tetragonal and orthorhombic symmetries and found no significant differences for the two models. For simplicity, we show the results for the tetragonal model. It is also important to note that the transverse acoustic modes C_{44} and $(C_{11}-C_{12})/2$ show elastic softening with decreasing temperature upon approaching T_{N1} [Fig. 1(c)]. Elastic softening reflects a coupling of the ultrasonic strain to quadrupolar degrees of freedom. With decreasing temperature, quadrupolar interactions strengthen, i.e., quadrupolar moments attempt to order. This produces a lattice distortion in a way to minimize the quadrupole-quadrupole coupling, which leads to elastic softening. Therefore, our experimental observations suggest sizable quadrupolar interactions for Er_3Al_2. We take them into account by using the following effective Hamiltonian:

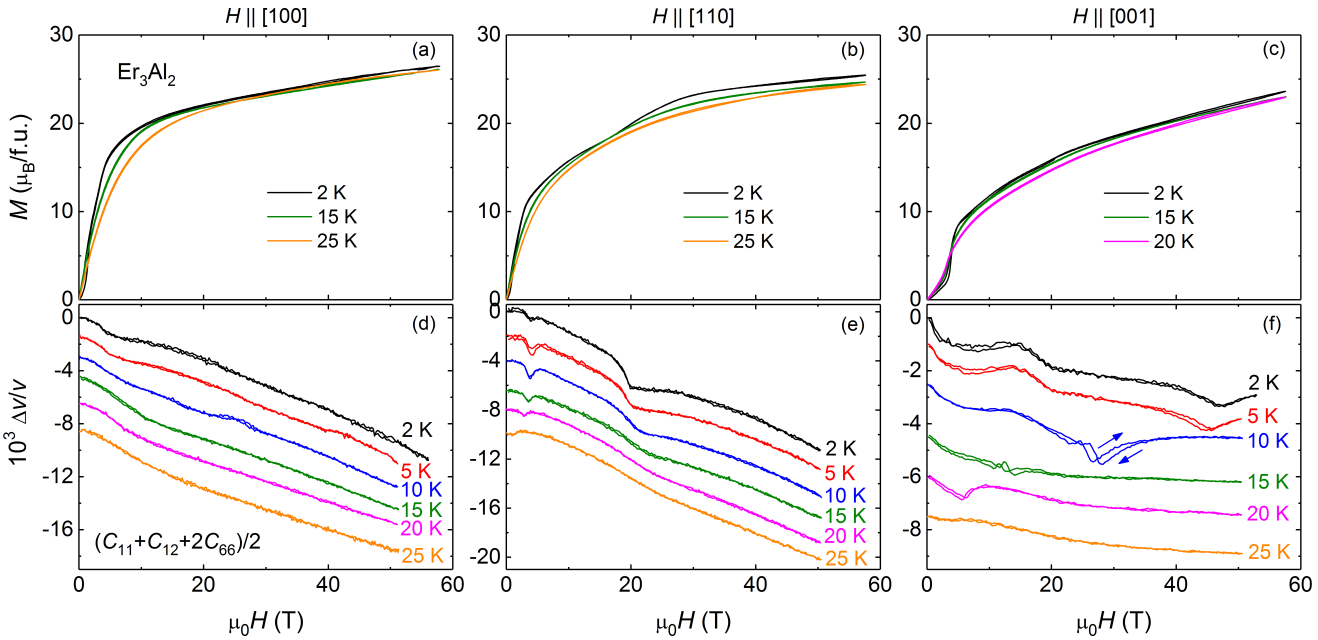

FIG. 3: Field dependences of the magnetization, M, and relative sound velocity, $\Delta v/v$, of longitudinal acoustic waves for field applied along the (a), (d) [100]; (b), (e) [110]; and (c), (f) [001] axes of Er_3Al_2 between 2 and 25 K. The ultrasound frequencies were 36, 42, and 82 MHz for field applied along the [100], [110], and [001] axes, respectively. In panels (d), (e), and (f), the curves are vertically shifted for clarity.

$$H_{\rm eff} = H_{\rm CEF} + H_{\rm sQ} + H_{\rm QQ} + H_{\rm Zeeman}, \quad (1)$$

where $H_{\rm CEF}$, $H_{\rm sQ}$, $H_{\rm QQ}$, and $H_{\rm Zeeman}$ are the CEF, strain-quadrupole, quadrupole-quadrupole, and Zeeman energy, respectively. The CEF term in the tetragonal symmetry is given by

$$H_{\rm CEF} = B_2^0 O_2^0 + B_4^0 O_4^0 + B_4^4 O_4^4 + B_6^0 O_6^0 + B_6^4 O_6^4, \quad (2)$$

where B_m^n are crystal-field parameters and O_m^n are Stevens' equivalent operators tabulated in Ref. [17]. Determination of the B_m^n is the goal of the analysis. The strain-quadrupole interaction is given by

$$H_{\rm sQ} = -\sum_i g_i O_i \varepsilon_i, \quad (3)$$

where g_i is the strain-quadrupole coupling constant, O_i is the quadrupole operator, and ε_i is the strain. The quadrupole-quadrupole interaction can be expressed as

$$H_{\rm QQ} = -\sum_i g_i' \langle O_i \rangle O_i, \quad (4)$$

where g_i' is the quadrupole-quadrupole coupling constant and $\langle O_i \rangle$ is a thermal average of the operator O_i. The Zeeman energy is

$$H_{\rm Zeeman} = -g_j \mu_{\rm B} J H. \quad (5)$$

As a first step in the analysis, we calculated the matrix elements of the nonperturbed Hamiltonian, $H_{\rm CEF} + H_{\rm Zeeman}$. Then, we included the quadrupolar interactions as a perturbation by adding the second and third terms of Eq. (1). The total elastic free energy is given by

$$F_{\rm total} = F_{4f} + \frac{1}{2} C_{ii}^{(0)} \varepsilon_i^2, \quad (6)$$

where the first term is the contribution of the Er $4f$ electrons and the second term is the contribution of the crystal lattice and electrons other than the $4f$ electrons. $C_{ii}^{(0)}$ is the background stiffness. The elastic modulus is defined by the second-order partial derivative of $F_{\rm total}$ with respect to the strain ε_i:

$$C_{ii}(T) = \left(\frac{\partial^2 F_{\rm total}(\varepsilon_i, T)}{\partial \varepsilon_i^2} \right)_{\varepsilon_i \to 0} = \\ = C_{ii}^{(0)}(T) - \frac{N_0 g_i^2 \chi_i^{(s)}(T)}{1 - g_i' \chi_i^{(s)}(T)}, \quad (7)$$

where strain-quadrupole and quadrupole-quadrupole interactions are taken into account. $N_0 = 8.055 \times 10^{27}$ is the number of Er^{3+} ions per unit volume. $\chi_i^{(s)}$ is the strain susceptibility that reflects mainly the quadrupolar character of the lowest CEF levels [1]. For the relative sound-velocity changes for the modes $(C_{11} - C_{12})/2$ and C_{44}, we used the relation $\frac{\Delta v}{v} = \frac{\Delta C}{2C}$. The strain corresponding to the $(C_{11} + C_{12} + 2C_{66})/2$ mode does

TABLE I: CEF parameters, B_m^n (K), for Er_3Al_2.

B_2^0	B_4^0	B_4^4	B_6^0	B_6^4
0.42(5)	0.004(5)	-0.022(5)	-1.5(5)×10^{-6}	9.0(5)×10^{-5}

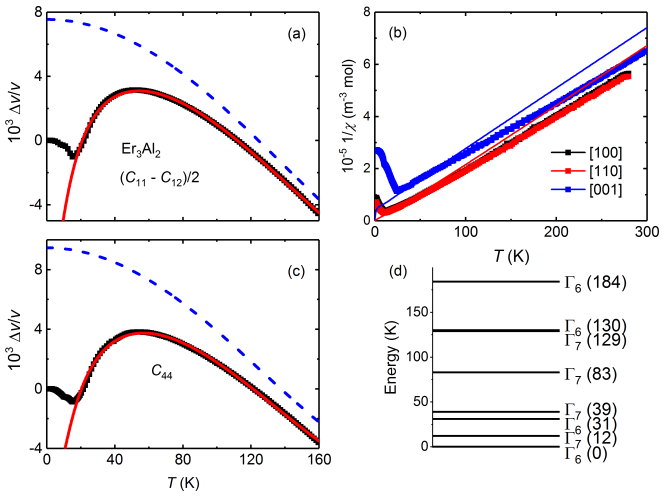

FIG. 4: Temperature dependences of (a) and (c) the relative sound-velocity changes, $\Delta v/v$, for the transverse acoustic modes $(C_{11} - C_{12})/2$ and C_{44}, respectively, and (b) the inverse magnetic susceptibility, $1/\chi$. (d) CEF level scheme of an Er^{3+} ion in Er_3Al_2 obtained from the CEF parameters listed in Table I. In panels (a), (b), and (c), the symbols and the solid lines represent the experimental and calculated data, respectively. The dashed lines in panels (a) and (c) represent the background stiffness. In panel (d), all horizontal lines correspond to doublets.

not linearly couple to quadrupolar degrees of freedom, which makes calculation of the sound velocity for this mode challenging. This mode could be estimated using the relation $C_{11} - (C_{11} - C_{12})/2 + C_{66}$, but we have no data for C_{11} and C_{66}. Additionally, we verified our CEF parameters by reproducing the temperature and field dependences of the magnetic susceptibility and magnetization [18].

For the CEF parameters listed in Table I, we could describe the elastic and magnetic properties of Er_3Al_2 in the paramagnetic state. Our analysis reproduces the softening of $\Delta v/v$ for $(C_{11} - C_{12})/2$ and C_{44} [Figs. 4(a) and (c)]. Here, we approximated the background stiffness using the expression $\frac{\Delta C^{(0)}}{C^{(0)}} = a + bT^2 + cT^4$, where the second and third term are the electron and phonon contribution, respectively [19]. The a, b, and c parameters as well as the g_i and g_i' constants are listed in Table II. The negative value of the quadrupole-quadrupole coupling constant, $g_i' = -0.0133(5)$ K, points to antiferroquadrupolar-type interactions for the quadrupole O_2^2 since it couples to the strain corresponding to the elastic mode $(C_{11} - C_{12})/2$. For C_{44}, we obtain $g_i' = 0.0183(5)$ K, which suggests ferroquadrupolar interactions for the O_{yz} and O_{zx} quadrupoles that couple to the strain of this acoustic mode. Our model also provides

TABLE II: Fit parameters obtained using Eq. (7).

Parameter	$(C_{11} - C_{12})/2$	C_{44}
a	0.0076(5)	0.0095(5)
b (K^{-2})	$-0.563(5) \times 10^{-6}$	$-0.625(5) \times 10^{-6}$
c (K^{-4})	$4.855(5) \times 10^{-12}$	$0.655(5) \times 10^{-12}$
$\lvert g_i \rvert$ (K)	15.89(5)	21.96(5)
g_i' (K)	-0.0133(5)	0.0183(5)

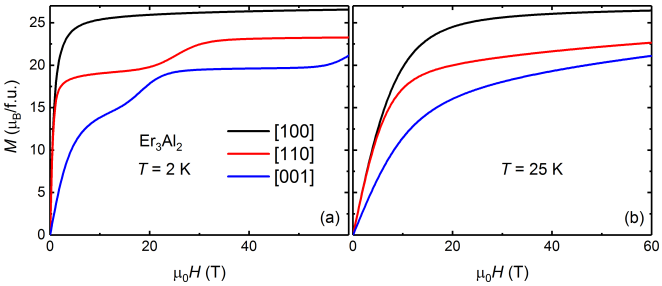

FIG. 5: Field dependences of the magnetization, M, at (a) 2 and (b) 25 K calculated for Er_3Al_2 using the CEF parameters listed in Table I.

a reasonable agreement with experiment for the inverse magnetic susceptibility, $1/\chi$ [Fig. 4(b)]. The CEF model produced a somewhat different slope, which is likely due to a single Er^{3+} crystallographic site assumed by the model, whereas three inequivalent positions for Er^{3+} are present in the crystal structure of Er_3Al_2 [12, 13].

Based on our analysis, we propose the following CEF scheme. In the tetragonal CEF, the 16-fold mutiplet of an Er^{3+} ion splits into eight doublets [Fig. 4(d)]. The ground-state doublet Γ_6 is separated from the first excited doublet Γ_7 by 12 K. The next levels are Γ_6 and Γ_7 at 31 and 39 K, respectively. The overall splitting up to the highest level is just about 184 K.

It should be noted that all levels are Kramers doublets. The ground-state doublet has no quadrupolar degeneracy and cannot explain the softening of $\Delta v/v$ for $(C_{11} - C_{12})/2$ and C_{44}. This means, the matrix elements $\langle\Gamma_6|O_2^2|\Gamma_6\rangle$, $\langle\Gamma_6|O_{yz}|\Gamma_6\rangle$, and $\langle\Gamma_6|O_{zx}|\Gamma_6\rangle$ are zero. However, the lowest excited levels are close to the ground state, which makes interlevel interactions possible. For example, the matrix elements for the quasi-quartet state formed by the ground state and the first excited state, $\langle\Gamma_6|O_2^2|\Gamma_7\rangle$, $\langle\Gamma_6|O_{yz}|\Gamma_7\rangle$, and $\langle\Gamma_6|O_{zx}|\Gamma_7\rangle$, are nonzero. This explains the quadrupolar interactions detected by our sound-velocity measurements for the acoustic modes $(C_{11} - C_{12})/2$ and C_{44}.

Our model also qualitatively reproduces the field-dependent magnetization. The data in the paramagnetic state do not show CEF transitions explicitly [Fig. 5(b)], whereas there are a number of anomalies in the antiferromagnetic state [Fig. 5(a)]. At 2 K, the magnetization for field applied along the [100] axis grows quickly up to 25 μ_B/f.u. below 10 T and changes very little above 10 T. When field is applied along the [110] direction, a CEF

transition becomes resolvable near 20 T. Experimentally, we observe an anomaly just below 20 T [Fig. 2(a)]. For $\boldsymbol{H}$ || [001], the model shows transitions between 10 and 20 T and around 60 T. Although the experimentally measured magnetization increases more smoothly in this field range, the sound velocity shows a change of slope near 20 T and a minimum between 40 and 50 T [Fig. 2(b)]. Therefore, the anomalies in $\Delta v/v$ could be interpreted as CEF transitions.

For a more detailed analysis of the magnetic and elastic properties of Er_3Al_2, a refined model is necessary. The present analysis could be extended by taking into account all three crystallographic positions of Er^{3+} ions and determining the exchange coupling constants between them. However, the most straightforward way to determine CEF parameters is to use inelastic neutron scattering in combination with another experimental technique, e.g., magnetic-susceptibility measurements [20].

IV. CONCLUSION

We studied the magnetic and elastic properties of Er_3Al_2 and observed three antiferromagnetic phase transitions at 10, 14, and 24 K. In pulsed magnetic fields up to 58 T, the magnetization and sound velocity show a number of anomalies. The critical fields of some of them do not change with temperature, which suggests their CEF origin. A CEF model that takes quadrupolar interactions into account explains most of these anomalies. Additionally, it reproduces the elastic softening detected for the velocity of transverse acoustic waves with decreasing temperature in the paramagnetic state. However, not all features are described by the model. A refined description that considers all three crystallographic positions of Er^{3+} ions and the exchange interactions between them seems to be needed.

V. ACKNOWLEDGMENTS

We acknowledge the support from HLD at HZDR, member of the European Magnetic Field Laboratory (EMFL), from DFG through Würzburg-Dresden Cluster of Excellence on Complexity and Topology in Quantum Matter-*ct.qmat* (EXC 2147, project-id 39085490). This work was supported by JSPS KAKENHI Grant Numbers 17H06136, 18KK0078, and 19K03719, the grant 21-09766S of the Czech Science Foundation, and the Materials Growth and Measurement Laboratory (MGML, https://mgml.eu).

[1] P. Morin and D. Schmitt, in *Handbook of Magnetic Materials*, edited by K. H. J. Buschow, Vol. 5 (Elsevier, Amsterdam, 1990), p. 1.

[2] D. Gignoux and D. Schmitt, in *Handbook of Magnetic Materials*, edited by K. H. J. Buschow, Vol. 10 (Elsevier, Amsterdam, 1997), p. 239.

[3] Q. Si and F. Steglich, Heavy fermions and quantum phase transitions, Science **329**, 1161 (2010).

[4] J. S. Gardner, M. J. P. Gingras, and J. E. Greedan, Magnetic pyrochlore oxides, Rev. Mod. Phys. **82**, 53 (2010).

[5] D. Gignoux and D. Schmitt, Competition between commensurate and incommensurate phases in rare-earth systems: Effects on *H-T* magnetic phase diagrams, Phys. Rev. B **48**, 12682 (1993).

[6] J. García Soldevilla, J. A. Blanco, J. Rodríguez Fernández, J. I. Espeso, J. C. Gómez Sal, M. T. Fernandez-Díaz, J. Rodríguez-Carvajal, and D. Paccard, Complex magnetic ordering in $NdNi_{1-x}Cu_x$: Determination of the magnetic structure by neutron diffraction, Phys. Rev. B **70**, 224411 (2004).

[7] K. Prokeš, E. Muñoz-Sandoval, A. D. Chinchure, and J. A. Mydosh, Competing magnetic structures and magnetic transitions in Er_2Ni_2Pb: Powder neutron diffraction measurements, Phys. Rev. B **78**, 014425 (2008).

[8] P. Čermák, K. Prokeš, B. Ouladdiaf, M. Boehm, M. Kratochvílová, and P. Javorský, Magnetic structures in the magnetic phase diagram of Ho_2RhIn_8, Phys. Rev. B **91**, 144404 (2015).

[9] T. Onimaru, Y. F. Inoue, K. Shigetoh, K. Umeo, H. Kubo, R. A. Ribeiro, A. Ishida, M. A. Avila, K. Ohoyama, M. Sera, and T. Takabatake, Giant uniaxial anisotropy in the magnetic and transport properties of $CePd_5Al_2$, J. Phys. Soc. Jpn. **77**, 074708 (2008).

[10] I. Ishii, K. Takezawa, T. Mizuno, S. Kumano, T. Suzuki, H. Ninomiya, K. Mitsumoto, K. Umeo, S. Nakamura, and S. Ohara, Anisotropic phase diagram of ferroquadrupolar ordering in the trigonal chiral compound $DyNi_3Ga_9$, Phys. Rev. B **99**, 075156 (2019).

[11] D. I. Gorbunov, I. Ishii, Y. Kurata, A. V. Andreev, T. Suzuki, S. Zherlitsyn, and J. Wosnitza, Crystal-field effects in $Er_3Ru_4Al_{12}$ with a distorted kagome lattice, Phys. Rev. B **101**, 094415 (2020).

[12] R. L. Davis, R. K. Day, J. B. Dunlop, and B. Barbara, Structure (Neutron) of Er_3Al_2, Acta Cryst. **C43**, 1675 (1987).

[13] R. L. Davis, R. K. Day, J. B. Dunlop, and B. Barbara, Magnetic structures of Er_3Al_2, Mater. Sci. Forum **27-28**, 249 (1988).

[14] Y. Skourski, M. D. Kuz'min, K. P. Skokov, A. V. Andreev, and J. Wosnitza, High-field magnetization of Ho_2Fe_{17}, Phys. Rev. B **83**, 214420 (2011).

[15] B. Lüthi, *Physical Acoustics in the Solid State* (Springer, Heidelberg, 2005).

[16] S. Zherlitsyn, S. Yasin, J. Wosnitza, A. A. Zvyagin, A. V. Andreev, and V. Tsurkan, Spin-lattice effects in selected antiferromagnetic materials (Review Article), Low Temp. Phys. **40**, 123 (2014).

[17] M. T. Hutchings, Point-charge calculations of energy levels of magnetic ions in crystalline electric fields, Solid State Physics **16**, 227 (1964).

[18] N. V. Hieu, T. Takeuchi, H Shishido, C. Tonohiro, T. Yamada, H. Nakashima, K. Sugiyama, R. Settai, T. D.

Matsuda, Y. Haga, M. Hagiwara, K. Kindo, S. Araki, Y. Nozue, and Y. Onuki, Magnetic properties and crystalline electric field scheme in RRhIn$_5$ (R: Rare Earth), J. Phys. Soc. Jap. **76**, 064702 (2007).

[19] M. Nohara, T. Suzuki, Y. Maeno, T. Fujita, I. Tanaka, and H. Kojima, Unconventional lattice stiffening in superconducting $La_{2-x}Sr_xCuO_4$ single crystals, Phys. Rev. B **52**, 570 (1995).

[20] P. Morin and J. A. Blanco, Determination of the crystalline electric field in the tetragonal symmetry rare earth intermetallic $HoAg_2$, J. Magn. Magn. Mater. **119**, 59 (1993).